POLITECNICO DI TORINO
Repository ISTITUZIONALE

Application of A* algorithm for microstructure and transport
properties characterization from 3D rock images

(Article begins on next page)

11 April 2024

Application of A* algorithm for microstructure and transport properties characterization from 3D rock images

Eloisa Salina Borello [a], [*], Costanzo Peter [b], Filippo Panini [a], Dario Viberti [a]

[a] Politecnico di Torino, Corso Duca degli Abruzzi 24, 10129, Turin, Italy
[b] Center for Sustainable Future Technologies, Via Livorno 60, 10144, Turin, Italy

ARTICLE INFO

ABSTRACT

Thorough comprehension of flow behavior in underground porous media is fundamental for several applications such as oil and gas production, Underground Gas Storage, CO2 storage, and Enhanced Geothermal Systems. Macroscale petrophysical parameters, as well as hydraulic parameters, are strongly linked to the microstructure of the rock.

In this paper, we present a methodology for the geometric analysis and characterization of the pore structure of 3D binary images of rocks. The geometric analysis is based on the A* pathfinding algorithm extended to 3D domains and on the measurement of the pore radius along the identified paths. The analysis is carried out for the main flow directions to obtain a tensorial representation of tortuosity, effective porosity, and representative pore radius, to provide permeability estimation and effective characterization of anisotropy. Moreover, the approach provides the analysis of pore size distribution and constriction.

The methodology was applied to synthetic but realistic rock samples, generated through the QSGS algorithm. Two case studies, representative of an isotropic and an anisotropic porous media, are presented. Validation was carried out through comparison with FVM hydrodynamic modeling. Analysis of the results shows that the presented geometric approach can provide thorough and reliable characterization of the porous media.

1. Introduction

The definition of an optimal reservoir management strategy is fundamental for several applications such as oil and gas primary production, Enhanced Oil Recovery, Underground Gas Storage, CO2 storage, and/or Enhanced Geothermal Systems [1–3], and it requires thorough understanding of fluid flow phenomena dominating reservoir behavior. Furthermore, several aspects related to economical, technical, and environmental issues [4] must be taken into account in view of an integrated study. All the information provided by technical disciplines (such as geology, geophysics, log interpretation, laboratory measurements for fluid PVT and rock properties characterization, well testing, reservoir engineering, and geomechanics) must be compared, combined, and properly integrated for a correct description and deep understanding of the

reservoir dynamic behavior [5–13]. Furthermore, the associated uncertainty must be estimated [14–16] and, possibly, mitigated by the acquisition of further information at all stages of reservoir life.

In this view, characterization, and analysis of fluid flow phenomena at micro and macro scales in underground porous media is a fundamental piece of information that can contribute to maximizing reservoir dynamic behavior understanding by minimizing uncertainties in the characterization of rock fluid interaction parameters. Macroscale parameters and corresponding fluid dynamic behavior are strongly affected by the micro geometric features of the pore space. In many cases, the flow mechanism can be understood from pore scale phenomena, allowing predictions at macro scale, which can be compared with experimental results [17]. The fluid flow at macro scale is modeled by averaging the microscopic continuity and momentum equations over a Representative Elementary Volume (REV) [17], adopting a parametrization mainly based on porosity and permeability [18]. Under the assumption of small Reynolds numbers Darcy's equation is adopted [17]:

* Corresponding author. DIATI Department, Politecnico di Torino, C.so Duca degli Abruzzi 24, 10129, Turin, Italy.
E-mail address: eloisa.salinaborello@polito.it (E. Salina Borello).

$$u = -\frac{k}{\mu}\nabla p \tag{1}$$

where u is Darcy's velocity, μ the viscosity, k the permeability, and ∇p the pressure gradient.

Natural porous media are extremely complex systems characterized by tortuous structure and significant variability of grains and pore sizes [18]. Tortuosity (τ) was introduced by Carman [19] to address the convoluted fluid paths in the pore structure. Currently, two main types of tortuosity are discussed in the literature: geometric tortuosity (τ_g) calculated based on the shortest length between inlet and outlet avoiding the solid obstacles [20,21]; hydraulic tortuosity (τ_h) based on the effective fluid path length [19].

The effective porosity (ϕ_e), was introduced to quantify the interconnected pore space covered by the flow [22]:

$$\phi_e = \frac{V_{flow}}{V_b} \tag{2}$$

where V_{flow} is the conductive pore space and V_b is the bulk volume.

The Kozeny-Carman equation [19,23] is the most used relationship to express the permeability as a function of the pore structure parameters:

$$k = \frac{\phi r_h^2}{c_K \tau^2} \tag{3}$$

where c_K is the Kozeny-Carman coefficient and r_h is the hydraulic radius, which is representative of the average pore radius.

Furthermore, Berg [24] quantified the reduction in permeability due to the variation in pore cross-sectional area (A) along the pore channel length (L_p) by introducing the constriction factor (C):

$$C = \frac{1}{L_p^2} \int_0^{L_p} A(x)^2 dx \int_0^{L_p} \frac{1}{A(x)^2} dx \tag{4}$$

Several geometric approaches for pore network characterization, based on 2D or 3D image analysis, are discussed in the literature. Since a complete review of the available methods is beyond the scope of this paper, a selection of the main approaches identified by the authors is listed here for the readership's convenience. Segmentation based algorithms, such as grain recognition ([68]), watershed ([25–27] and references therein) and morphology segmentation [28], allow determination of the pore connectivity and calculation of the pore radius on segmented pore portions, distinguishing between pore radius and pore throat. The fractal geometry approach [29–31], and percolation theory ([32] and references therein) are mainly used for total porosity and permeability estimation. Algorithms for pore skeleton extraction such as medial-axis [33], medial surface [34], and thinning process [35] can be coupled with post-processing routines for pore radius estimation [35] as well as with connected paths search for tortuosity estimation [34]. Application of pathfinding approaches, such as Dijkstra's algorithm [36], directly provides the connected paths in the desired direction and is therefore well suited for tortuosity estimation. However, the Dijkstra algorithm is computationally expensive even when applied to small images [37].

In this paper, we applied a methodology based on the pathfinding algorithm A*, which significantly outperformed the Dijkstra algorithm on 2D random octile grids [38].

The A* algorithm was extended to 3D domains to identify connected paths for the main flow directions (x, y, z). Furthermore, along each identified path, the vector containing local pore size (r_p) is obtained by approximating the local pore area with an ellipses orthogonal to the local path direction, providing reliable information for a thorough description, analysis and characterization of the internal geometry of the porous medium. This is an added value with respect to CFD simulation, which does not provide a detailed geometrical analysis of the pore structure. Some of the possible applications include effective diffusion coefficient calculation, evaluation of the effect of weathering in ornamental stones, and estimation of petrophysical properties. As a consequence, it can be useful in a variety of scenarios such as geothermal applications, gas storage, both of CO_2 and H_2, and reservoir production.

It is possible to obtain a tensorial representation of tortuosity, effective porosity, and representative pore radius and constriction factor based on the characterization of the internal geometry of the porous medium. The tensorial representation allows permeability estimation for each principal direction and effective characterization of anisotropy. We applied the methodology to both isotropic and anisotropic 3D images of synthetic porous media generated by modifying the original Quartet Structure Generation Set algorithm (QSGS) presented in Ref. [39]. The results were validated by CFD numerical simulation, which is suitable for fluid flow simulation at the pore-scale in complex geometries [40].

2. Methodology description

The methodology is applied to a 3D binary description of a rock sample (grain = 0, void = 1), which can be obtained by image processing of an X-ray micro-tomography image. In this paper, we generated synthetic 3D binary samples through the random porous media generation algorithm Quartet Structure Generation Set (QSGS) [39]. We analyzed the pore structure by identifying the effective flow paths in single-phase conditions. Successively, we quantitatively characterized the porous medium in terms of pore constriction, effective porosity, tortuosity, permeability, and pore size distribution. In this paper, the pore size and the pore radius refer to the local aperture and the semi-aperture between the pore walls, respectively; pathways were assessed following two different approaches: the geometric approach based on the pathfinding algorithm A* and the hydrodynamic CFD simulation.

2.1. Generation of porous media

QSGS [39] is a method for generating 3D structures and internal morphology based on the stochastic cluster growth theory. QSGS generates microstructures of porous media such as rocks [41–43], and soils [44] in quite a realistic way with few control parameters. Three control parameters are required for a porous medium saturated by a single fluid: porosity (ϕ), core distribution probability (P) and a set of growth probabilities (D_i). The core distribution probability is the probability of a grid cell center to become the core of a grain. It determines the degree of detail of a structure. In fact, a bigger P leads to a higher number of smaller grains, less detailed in shape. The growth probability D_i is the probability of the grain to grow in the i-direction. The set of growth probabilities allows regulating the anisotropy aspect. In the 3D case, 26 directions (6 main, 12 side, and 8 diagonal; [66]) are considered. The adopted direction scheme is shown in Fig. 1, where main directions ($D_1 - D_6$) are depicted in green, side directions (D_7-D_{18}) in red and diagonal directions ($D_{19}-D_{26}$) in blue.

Isotropic structures are obtained by setting uniform values within each class of direction, main ($D_1 - D_6$), side (D_7-D_{18}), and diagonal ($D_{19}-D_{26}$) [45]. We adopted the following:
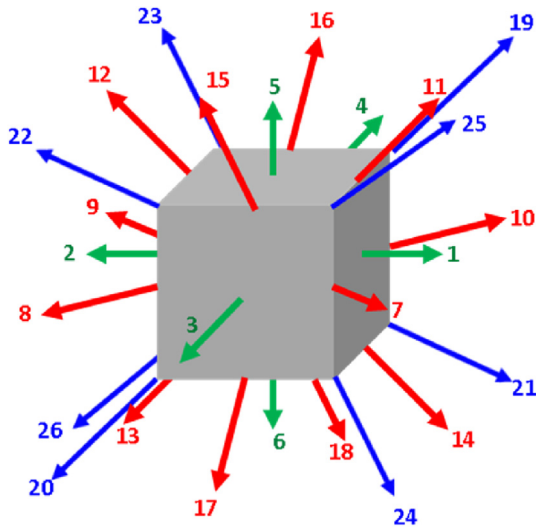
Fig. 1. Direction scheme in the 3D case: main directions D_1-D_6 (green), side directions D_7-D_{18} (red), and diagonal directions D_{19}-D_{26} (blue). (For interpretation of the references to colour in this figure legend, the reader is referred to the Web version of this article.)

$$D_1 - D_6 = D_1$$

$$D_7 - D_{18} = \frac{1}{12}D_1 \tag{5}$$

$$D_{19} - D_{26} = \frac{1}{8}D_7$$

To introduce vertical anisotropy, horizontal and vertical growth probabilities are linked to an aspect ratio $AR = D_z / D_{xy}$

$$D_1 - D_4 = D_1$$

$$D_5 - D_6 = AR\, D_1 , \ AR < 1$$

$$D_7 - D_{10} = \frac{1}{12}D_1 \tag{6}$$

$$D_{11} - D_{18} = \frac{\sqrt{AR}}{12}D_1$$

$$D_{19} - D_{26} = \frac{\sqrt[3]{AR}}{96}D_1$$

The resulting relationship between anisotropy, in terms of permeability, and growth probability aspect ratio AR is nonlinear. A similar behavior can be recognized from the data provided by Wang et al. [46].

More in detail, the QSGS algorithm follows two steps [43]:

1. Randomly distribute the grain cores in the grid according to core distribution probability (P):
   a. Assign a random number n_g to each grid cell;
   b. The cells having $n_g < P$ become grain cores.
2. Iteratively enlarge each existing grain (solid phase) in all directions according to D_i, until the porosity reaches the desired value (ϕ):
   a. New random numbers n_{gi} are assigned to all neighboring cells of the grain.

b. The neighboring cell in the i-direction will belong to the grain if $n_{gi} < D_i$.

Due to the randomicity characterizing the generation procedure, the same set of control parameters will produce different geometries sharing similar but not identical morphological features.

Recently, modified versions of QSGS were proposed to account for the multiscale pore size distribution [46,47,66]. Wang et al. [46] used a combination of a coarse and a refined structure obtained by two independent simultaneous construction processes, characterized by different core distribution probabilities (P_{coarse}, and $P_{refined}$, respectively). For the anisotropic case study, we adopted a modification of the two-scale generation method suggested by Wang et al. [46]. In our implementation, coarse and refined structures are constructed in sequence. Once the coarse grain structure G_1 is fully grown to a target porosity (ϕ_{coarse}), the refined grain structure G_2 is grown independently until the combination of the two structures (G_3) reaches the required porosity ϕ. The combined grain structure (G_3) is obtained by the union of the coarse and refined structures, with possible local compenetration. The flowchart of the proposed implementation is shown in Fig. 2. The obtained geometry may not be fully connected, i.e. there may be some occluded or isolated pores not connected with the main void space. In the considered cases $\phi_e / \phi \approx 0.85$, which is reasonable for sand rocks [48].

Let it be noted that QSGS gives a simplified representation of rock complexity even in the modified version. In fact, it assumes stationarity over the domain of interest, thus it is not able to reproduce heterogeneity. Moreover, unlike fractal approaches, it ignores the scale-invariance properties widely existing in porous media [49]. However, it is a comprehensive algorithm to characterize the original complexity in natural porous media, such as the random internal morphology and anisotropic properties [49].

2.2. Geometric characterization

The pore structure of each generated 3D binary image of porous media is characterized by adopting a path-finding approach. A set of n_{in} inlets and n_{out} outlets, corresponding to the centroids of a number of properly selected pixels, are placed along the boundary faces of the porous domain orthogonal to each main flow direction (x, y, or z) [50]. Since a manual selection of inlets and outlets would be time-consuming in 3D scenarios with low grainsize, an automatic selection procedure was also developed, which is reported in appendix A. For each direction, a path is searched for each combination between the selected n_{in} inlets and n_{out} outlets, giving $n_{in} \times n_{out}$ paths per direction. The A* algorithm is used to compute the shortest paths between each inlet-outlet pair [51,52]. The process is achieved by steps. Starting from an inlet location ($n=n_0$), at each step, the algorithm expands the current node n by exploring all nodes n_i, called successors, in the proximity of n. For each successor (n_i), n is set as the parent node and a cost function $c(n_i)$ is calculated as:

$$c(n_i) = g(n_i) + h(n_i) \tag{7}$$

where i indicates the i-th successor of n, $g(n_i)$ is the backward cost, i.e. the distance calculated over the incremental path already identified from the inlet to n_i, and $h(n_i)$ is the forward cost, i.e. a heuristic function representing the estimation of the cost to move from n_i to the target (outlet) (Fig. 3). We adopted the Euclidian distance as forward cost $h(n_i)$. The algorithm then moves from node n to the node which provides the lowest cost among all explored but unexpanded nodes (i.e. nodes for which cost function has already been computed but successors have not been explored). The calculation is repeated until the target is reached and the path
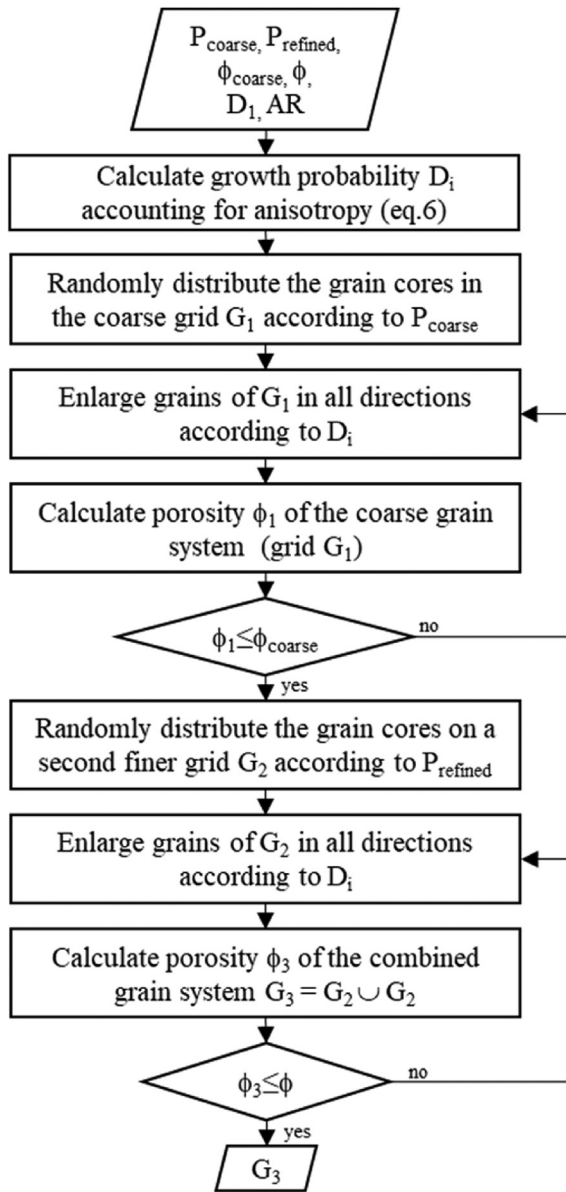
Fig. 2. Flow chart of the implemented anisotropic two-scale grain size distribution, based on QSGS.

is then built backward from the target to the inlet by connecting the parent nodes.

From the implementation point of view, two lists of nodes are created: the Open List, a structure that holds the explored but unexpanded nodes (their successors have not been explored yet); the Closed List, a structure that holds every expanded node (their successors have been already explored and included in the Open List). More algorithmic details are shown in the flow chart of Fig. 7.

It should be noted that the presence of obstacles (i.e. grains) could extend or interrupt the path development between the considered node and the target, thus Euclidean distance could give a wrong estimate of forward cost, therefore the selected direction at a certain step could be suboptimal, i.e. dead ends occur or $c(n_i)$ grows significantly for all the successors. In such cases, the algorithm can go back to a promising parent node and expand another successor node to calculate alternative promising paths. In fact, for each explored node (n_i) the cost value $c(n_i)$, as well as its parent node (n), are stored.

On finite graphs, convergence is guaranteed since the A* algorithm is complete [53], i.e. it will always find a path from the inlet to the outlet if at least one exists, and it is guaranteed to terminate if no path exists. Moreover, the solution is optimal if the heuristic function, used to estimate the forward cost, is admissible and monotonic [53]. The Euclidean distance is admissible because it never overestimates the path cost to the target (outlet). The Euclidean distance is also monotonic because the total estimated path cost (forward plus backward) of a successor is always greater than (or equal to) its parent cost.

The drawback of A* search is that it keeps all explored nodes in memory. Thus, its space complexity is $O(b^d)$ where d is the depth of the solution (i.e. number of nodes of the shortest path), and b is the branching factor which is the average number of successors expanded per state (i.e. grid node of the optimal path) [53]. The branching factor depends on the effectiveness of the heuristic function: the more accurate the estimate of the heuristics of the actual forward cost, the shorter the times the algorithm should go back to explore another way by expanding another node. Ideally b should be equal to 1. In other words, a good heuristic allows A* to prune away many of the b^d nodes that an uninformed search would expand.

The time complexity of A* is again related to the number of explored nodes $O(b^d)$ [53].

The overall time complexity of path tracking with A* in a porous medium depends also on the number of inlet/outlet pairs considered for each direction (x, y, z). Given the same number of inlet (n_{in}) and outlet (n_{ou}) points for each direction, overall time complexity becomes $O\left((n_{in} \, n_{ou})^3 b^d\right)$, where d increases with the sample dimension and the image resolution. Values of d and b are also sensitive to the complexity of the porous geometry and to the way the successors are constructed (Fig. 4). The number of successors explored at each depth depends on the connecting distance (c_d), which determines the number of directions explored (Fig. 4). We adopted $c_d = 1$, which in 3D corresponds to the exploration of 26 successor nodes. Connecting distance equal to 1 provides an optimal path with more nodes, generally in number equal or greater than the number of pixels in the investigated flow direction (Fig. 5b). However, from the point of view of the amount of overall explored nodes (Fig. 5a), no significant difference is observed with different connecting distances, since more nodes are explored at each path depth if the connecting distance increases (Fig. 5c). Moreover, a low connectivity distance does not allow any possible grain cross-cutting by an edge between two nodes, even in complex geometries.

Along each identified geometric path, the local pore size (r_p) is estimated. In 2D scenarios, the pore size is obtained as the pore extension orthogonal to the local path direction at each node identified by the algorithm [50]. In 3D scenarios, the orthogonal plane to the local path direction must be identified. The pore section is estimated locally in two directions, mutually perpendicular, belonging to the orthogonal plane (Fig. 6); further details are given in appendix B. The information provided by this methodology can be used for pore structure characterization in terms of tortuosity, pore constriction, representative pore radius, as well as effective porosity. All these properties are estimated for each principal direction (x, y, z). This way, possible differences in the effective pore space interested by the flow in different directions, as well as directional variations in pore structure (tortuosity, average pore radius, and pore constriction), can be highlighted. Based on those parameters, permeability and anisotropy can be estimated.

According to Wang et al. [46], an estimate of anisotropy can be obtained from the geometric analysis of the sample by computing the average pore number per unit length obtained from slices in
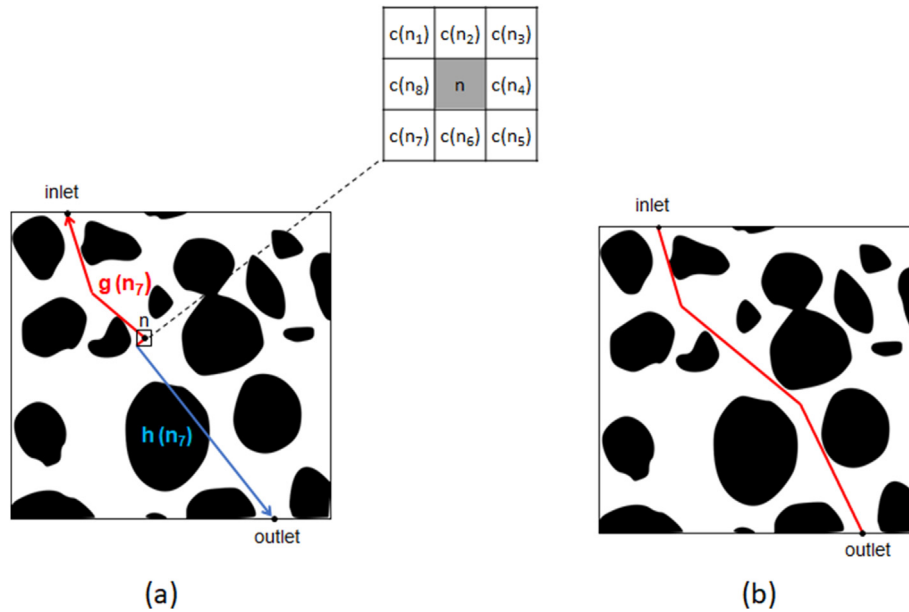
Fig. 3. Qualitative representation of A* cost-driving mechanism, shown in 2D for clarity: (a) cost function calculation where ***n*** represents the current path node, ***c***(n_1) - ***c***(n_8) are the cost functions calculated in the adjacent nodes 1−8 (successors), ***g***(n_7) and ***h***(n_7) are the backward and forward components for cost calculation of successor 7, respectively; (b) A* optimal path.

different directions, which is equivalent to:

$$\frac{k_{xy}}{k_z} = \frac{\sum_N w_i}{\sum_N h_i} \tag{8}$$

where w_i is the width, h_i is the height of the i-th pore and N is the total number of pores. However, in this approach directional variations in tortuosity, constriction, and effective porosity are not taken into account.

For permeability estimation, we started from the approach proposed by Mauran et al. [54], which extends the Kozeny-Carman equation (eq. (3)) to account for anisotropy by considering different values of texture parameters (effective porosity, and tortuosity) in the principal directions. We adopted effective porosity, and tortuosity from geometrical analysis and, in addition, we estimated a representative pore radius value for each principal direction. The permeability estimation becomes:

$$k_{g,i} = \frac{\phi_{eg,i}\, r_i^2}{c_k \tau_{g,i}^2} \text{ where } i = x, y, z \tag{9}$$

where $k_{g,i}$ is the permeability from the geometric calculation in the

i direction and c_k is the Kozeny-Carman coefficient, also called the shape factor; effective porosity $\left(\phi_{eg,i}\right)$, geometric tortuosity $(\tau_{g,i})$ and representative pore radius (r_i), are calculated geometrically by analyzing all the paths individuated across each direction $i = x,y,z$. Details are provided in the following.

Anisotropy (R) can thus be quantified either by the ratio of permeability in different directions or by Ref. [55]:

$$R = \frac{k_{min}}{\sqrt{k_{int} k_{max}}} \tag{10}$$

where k_{min} is the minimum permeability, k_{int} is the intermediate permeability and k_{max} is the maximum permeability value.

Since the path-finding approach is used to estimate representative pore radius, effective porosity (see eq. (11)) and tortuosity (see eq. (12)), eq. (9) allows the estimation of permeability and anisotropy based on a purely geometric analysis of the porous medium.

For each flow direction (i), the corresponding effective porosity was estimated through an extension of the purely geometric calculation based on path-finding presented in Ref. [50]:
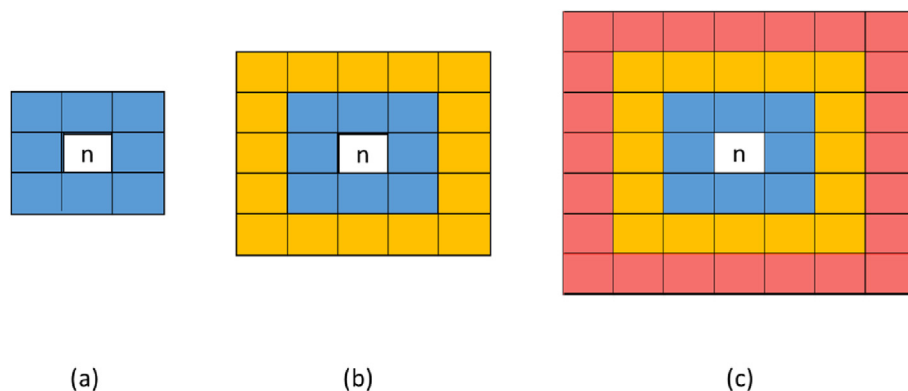

Fig. 4. Representation of successors construction in 2D for current node n with different connecting distances: (a) $c_d = 1$, (b) $c_d = 2$, (c) $c_d = 3$.
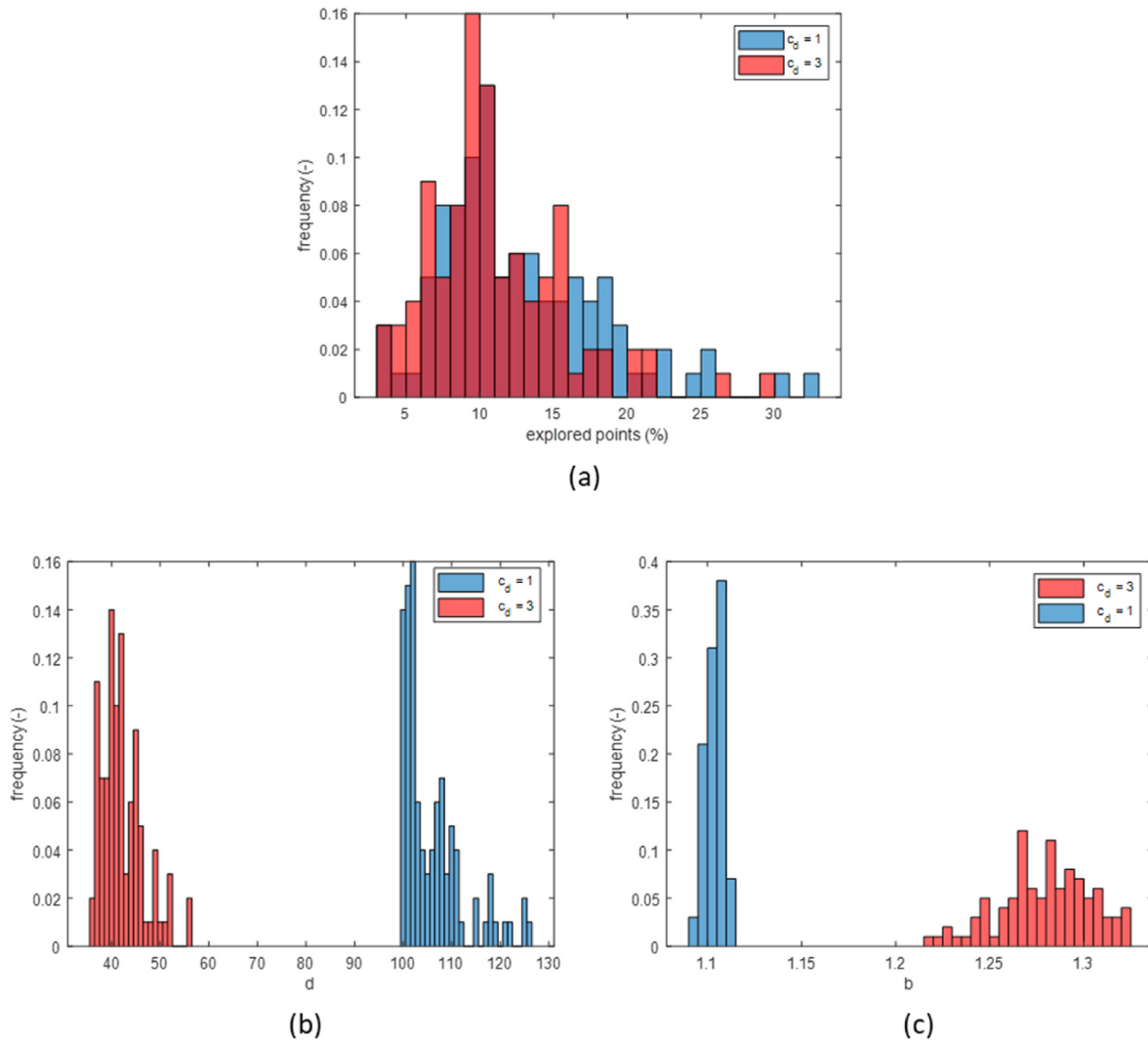
(a)

(b)

(c)

Fig. 5. Preliminary analysis of the effect of connectivity distance on the amount of explored nodes (a), the obtained path depth (b), and the branching factor (c); (case 1, direction x, 100 paths).

$$\phi_{eg,i} = \frac{N_{pp,i}}{N_{px}} \text{ where } i = x, y, z \tag{11}$$

where $N_{pp,i}$ is computed as the total number of pixels of all the pore channels portions crossed by at least one path in the considered i-direction while N_{px} is the total number of pixels. Therefore, $\phi_{eg,i}$ is calculated considering all the paths identified in the i-direction. This effective porosity includes only the fraction of the total porosity which participates in the flow along the specified direction. The overall effective porosity ϕ_{eg} is estimated by considering all the paths in the three flow directions x, y and z. In particular, eq. (11) becomes $\phi_{eg} = N_{pp}/N_{px}$, where N_{pp} is calculated from the 3D logic matrix representing all the pixels of the pore channels portion crossed by at least one path in at least one flow direction.

For each flow direction (i), the geometric tortuosity τ_g, is computed as the ratio between the average of the shortest pathway lengths ($\langle L_{sh,i} \rangle$) and the length of the domain (L_i) [18]:

$$\tau_{g,i} = \frac{\langle L_{sh,i} \rangle}{L_i} \text{ where } i = x, y, z \tag{12}$$

Here we selected the median of the shortest path lengths in place of the average.

The selection of the representative pore radius to be applied in eq. (9) is a sensitive choice. Since the square radius appears in eq. (9), a small change in radius may correspond to a significant change in permeability estimate. Moreover, the pore radius is often characterized by a multimodal distribution [67,68]. For this reason, we fitted the pore radius data with a kernel distribution and extracted the mode. The selected value is then compared with the hydraulic radius, which for a 3D sample is calculated as [56]:

$$r_h = \phi \frac{V_b}{A_w} \tag{13}$$

where V_b is the bulk volume of the sample and A_w is the wetted surface, i.e. the grains-void interface. The wetted area was
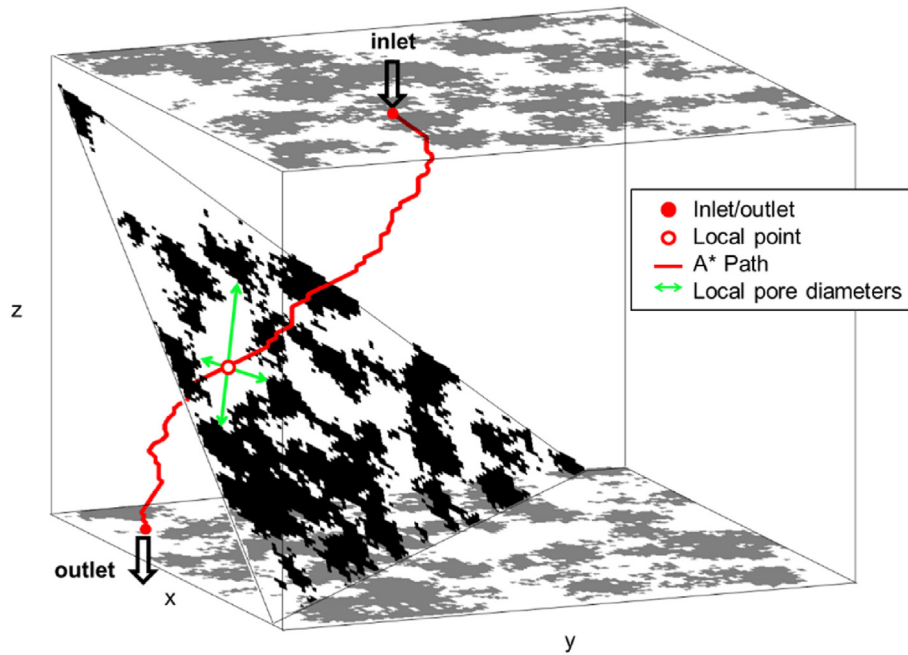
Fig. 6. Schematic representation of pore size estimation from the path-finding approach. Grains on top and bottom surfaces are represented in gray; grains on the slice normal to the local path are represented in black.

calculated with the open-source software ParaView on the 3D mesh of the solid grains by using the Integrate Variables filter, which computes the area of each mesh polygon and sums them up.

The Kozeny-Carman coefficient (c_k) is a dimensionless empirical geometric parameter in the range 4−40 [30] that depends on the porous media morphology and on the shape of the pores 2D cross-section perpendicular to the flow [57]. For well-structured porous media $c_k = 5$ is an acceptable value [17]; for fibrous porous media fractal analytical approach has been proposed [29,30]; however, for random porous media, c_k is generally determined by back-calculation of eq. (3) [22,54,57]. For isotropic scenarios, we assumed $c_k = 5.8$, as obtained in Koponen et al. [22] for an isotropic porous medium constituted by randomly distributed freely over-lapping squares. Conversely, for anisotropic scenarios, a different value must be considered, due to different pore geometry. As a consequence, for anisotropic or heterogeneous scenarios, c_k must be obtained by back-calculation.

Another texture parameter that can be assessed with the pro-posed geometric approach is the pore constriction (C), which rep-resents a decrease in permeability due to the variation of the cross-sectional area along the path (eq. (4)). By approximating every single path in the i-direction with a finite number of steps (n_p), one for each crossed pixel, and the local pore cross-section normal to the flow with a circle of equivalent radius r_e (see appendix B), eq. (4) becomes:

$$C_i = \frac{1}{n_p^2} \sum r_e(x,y,z)^4 \sum \frac{1}{r_e(x,y,z)^4} \qquad (14)$$

The mode $\overline{C}_i$ of constriction distribution is taken as a repre-sentative constriction factor for i-direction.

The geometric characterization workflow is summarized in form of a flow chart in Fig. 7.

2.3. Hydraulic characterization

Single-phase fluid flow was simulated by CFD modeling at low

Reynolds numbers (i.e. Re < 1) to obtain the hydraulic paths in the pore space. The CFD code OpenFOAM, based on the Finite Volume Method (FVM), was used for performing the simulations. The FVM is an effective technique for the computational modeling of single and multiphase fluid flow problems in porous media and for the evaluation of hydraulic tortuosity and permeability [40,43,58−60]. By using the native OpenFOAM mesh generator snappyHexMesh, a grid representing the pore space of the rock is created from the binary matrix obtained with the QSGS. Navier-Stokes equations (NSEs) govern the incompressible single-phase flow at small Rey-nolds numbers. The NSEs are solved for steady-state conditions by the Semi-Implicit Method for Pressure Linked Equations (SIMPLE) algorithm [61]. For each case study, three simulations were run to assess the textural parameters in each direction $i = x,y,z$. For each investigated direction (i), flow is forced toward i-direction by imposing a macroscopic pressure gradient ($\nabla_i p$) along such direc-tion. To this end, constant pressure at the inlet and at the outlet boundaries are imposed so that:

$$\nabla_i p = \frac{p_{in} - p_{out}}{L_i} \qquad (15)$$

where p_{in} is the imposed pressure at the inlet surface, p_{out} is the imposed pressure at the outlet surface and L_i is the sample length in the i-direction. No flow is imposed on the remaining external sur-faces while no-slip condition is imposed at the fluid-solid interface.

The hydraulic tortuosity in the i-direction was estimated from the simulated velocity values as [62]:

$$\tau_{h,i} = \frac{\langle |v| \rangle}{\langle v_i \rangle} \quad \text{where} \quad i = x,y,z \qquad (16)$$

where $|v| = \sqrt{v_x^2 + v_y^2 + v_z^2}$ is the magnitude of the local velocity, v_i is the directional component of the velocity and $\langle \rangle$ indicates the average over the void space. We verified that, under laminar flow, the estimated tortuosity is not sensitive to the imposed value of pressure gradient [63].

Fig. 7. Flow chart of geometric characterization.

Table 1
Analyzed cases generated with QSGS.

	Case 1	Case 2
$P(-)$	0.001	$P_{coarse} = 0.001$ $P_{refined} = 0.0001$
$D_{x,y}(-)$	0.001	0.001
$D_z (-)$	0.001	1e-9
ϕ (%)	30	$\phi_{coarse} = 50$ $\phi = 20$
r_h (µm)	4.25	5.03
Resolution (ppcm)	142.9	142.9

The effective porosity in the i-direction was calculated from the simulated velocity, by setting a threshold value on $|v|$: preliminary analysis on the velocity field distribution showed that velocities one order of magnitude smaller than $|v|$ did not significantly contribute to the fluid flow [50]. Consequently, the effective porosity is estimated as:

$$\phi_{eh,i} = \frac{N_{s,i}}{N_{tot}} \text{ where } i = x, y, z \tag{17}$$

where $N_{s,i}$ is the number of cells having the magnitude velocity above the threshold when flow is imposed in the i-direction and N_{tot} is the total number of cells. The overall effective porosity is estimated as $\phi_{eh} = N_s/N_{tot}$ where N_s is calculated from the 3D logic matrix representing all the cells having magnitude velocity above the threshold value in at least one simulated flow direction ($i = x, y, z$).

For each simulation, characterized by the imposed macroscopic pressure gradient $\nabla_i p$ in a certain direction $= x, y$ or z, the permeability ($k_{h,i}$) in the corresponding direction was directly calculated inverting Darcy's equation [40]:

$$k_{h,i} = -\frac{u_i \mu}{\nabla_i p} \text{ where } i = x, y, z \tag{18}$$

where u_i is the directional component of Darcy's velocity

$$u_i = \frac{1}{V} \int_V v_i(x, y, z) \, dV \tag{19}$$

with V the volume of the sample and $v_i(x, y, z)$ the local velocity field of the fluid in the i-direction.

3. Case studies

Two different case studies were considered: an isotropic case with 30% porosity (case 1) and an anisotropic case with a porosity of 20% and smaller grain sizes (case 2). Case 1 was generated with QSGS [39], while case 2 was generated with the modified two-scale version of QSGS (Fig. 2). QSGS parameters are listed in Table 1. The generated samples are logic matrixes, with $100 \times 100 \times 100$ pixels. The edge length was assumed to be 0.7 mm. The 3D images for case 1 and case 2 are shown in Fig. 8. 2D sections in the x, y, and z directions are shown in Fig. 9 and Fig. 10 for case 1 and case 2 respectively.

The mesh was refined for CFD simulation to guarantee at least 3−4 cells in the smallest pores. The invariance of the hydraulic
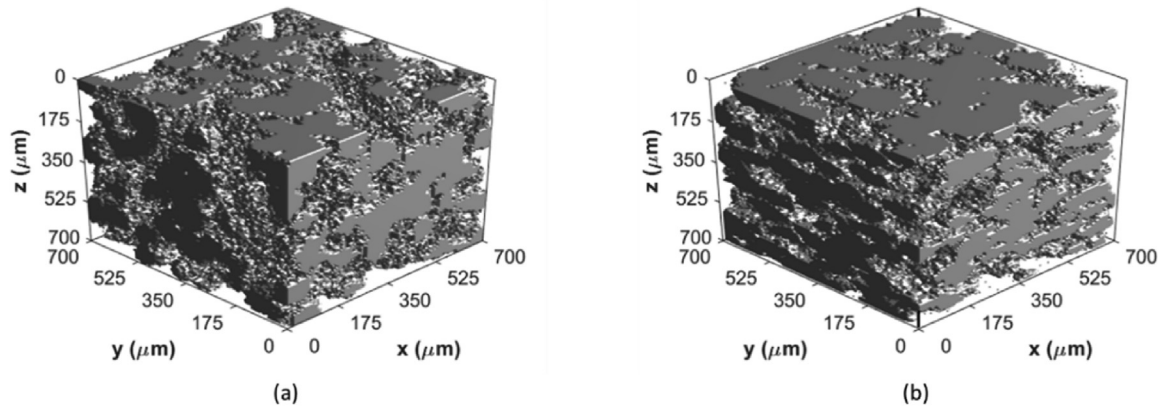

Fig. 8. 3D image of analyzed cases generated with QSGS: (a) isotropic (case 1) and (b) anisotropic (case 2).
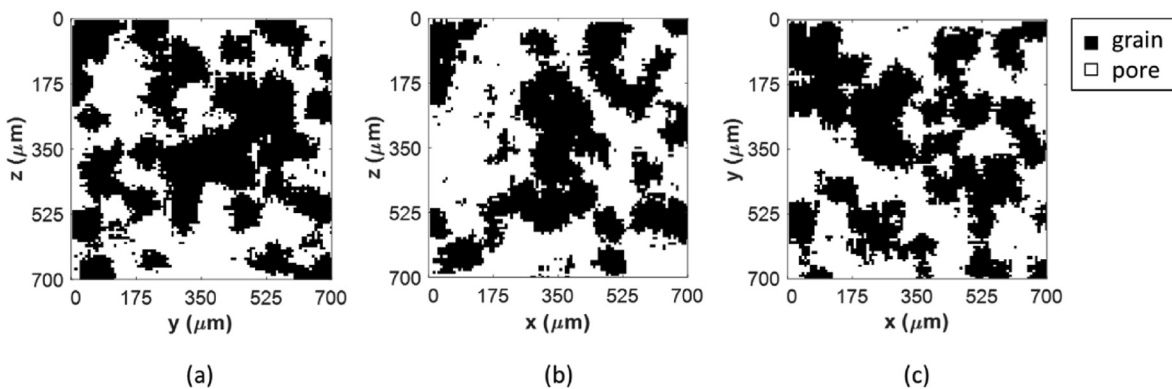

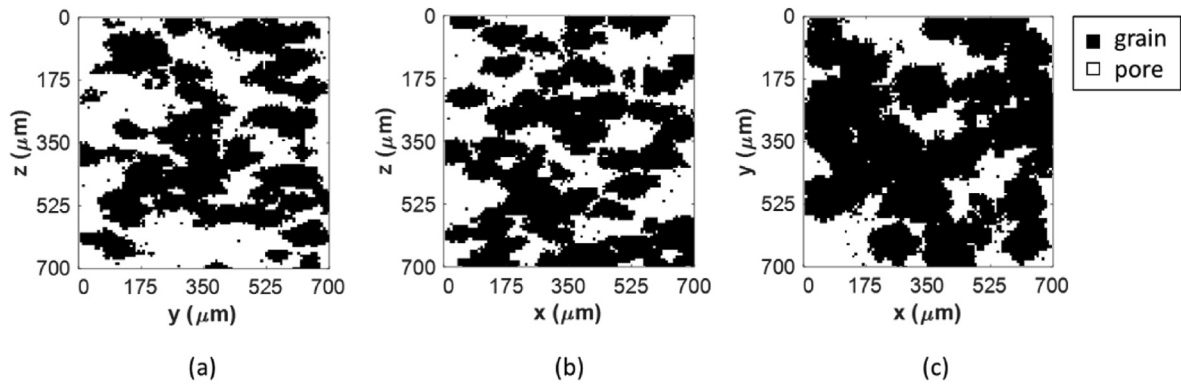**Fig. 9.** 2D top sections of case 1: (a) x, (b) y and (c) z direction.

Fig. 10. 2D top sections of case 2: (a) **x**, (b) **y** and (c) **z** direction.

Table 2
Fluid and fluid flow properties adopted for the hydraulic characterization.

	water	methane	heavy oil
μ (Pa s)	0.0005	1.60E-05	0.5
ρ (kg/m³)	1050	107.5514	1050
Δp (*Pa*)	0.0708	0.0708	0.0708
$\Delta p/L$ (*Pa/m*)	101.1429	101.1429	101.1429
Re	~10^{-4}	~10^{-2}	~10^{-10}

characterization was verified in single-phase fluid flow conditions with three different fluids: water, methane, and heavy oil. Different fluid properties were adopted in order to reproduce the behavior at reservoir conditions (150 bar, 45 °C) of the three fluids. In all the cases, the same pressure gradient between the inlet and the outlet was applied, assuring Reynolds number $Re \ll 1$. Details are given in Table 2.

Table 3
Comparison of results obtained with the geometric and hydrodynamic approaches (fluid = water).

|		Geometric	Hydrodynamic
Case 1	τ_x (−)	1.35	1.653
	τ_y (−)	1.38	1.660
	τ_z (−)	1.4	1.443
	φ_{ex}(%)	16.7	16.84
	φ_{ey}(%)	16.9	16.83
	φ_{ez}(%)	19.0	17.26
	φ_e(%)	24.9	26.32
	r_x (μm)	6.9	−
	r_y (μm)	7.2	−
	r_z (μm)	7.3	−
	C_x	187	−
	C_y	120	−
	C_z	125	−
	k_x (mD)	759	900
	k_y (mD)	807	764
	k_z (mD)	906	839
	k_x/k_z (−)	0.84	1.1
	k_y/k_z (−)	0.89	0.9
	R (−)	0.89	0.88
Case 2	τ_x (−)	1.52	1.320
	τ_y (−)	1.48	1.519
	τ_z (−)	1.73	2.068
	φ_{ex}(%)	12.4	11.02
	φ_{ey}(%)	11.25	10.57
	φ_{ez}(%)	9.65	11.05
	φ_e(%)	16.35	16.97
	r_x (μm)	15.5	-
	r_y (μm)	10.5	-
	r_z (μm)	8.5	-
	C_x	86	-
	C_y	94	-
	C_z	222	-
	k_x (mD)	653	663
	k_y (mD)	287	287
	k_z (mD)	118	72
	k_x/k_z (−)	5.5	9.3
	k_y/k_z (−)	2.4	4.0
	R (−)	0.27	0.16
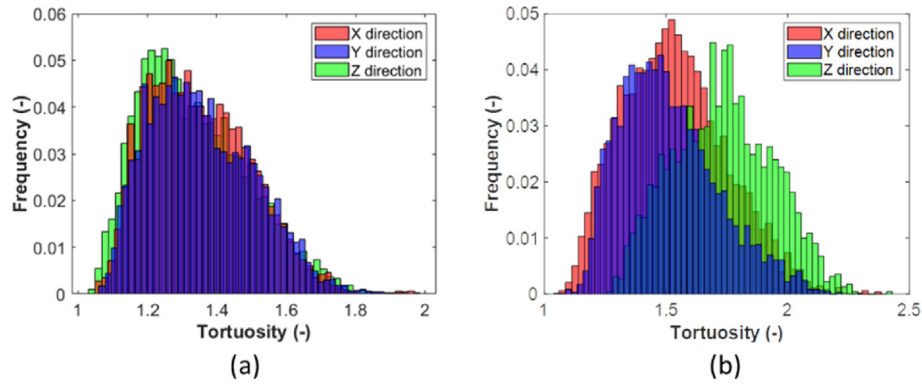
Fig. 11. Tortuosity distribution obtained from the geometric analysis for each flow direction: (a) case 1; (b) case 2.

4. Results and discussion

Results obtained from both geometric and hydraulic characterization are summarized in Table 3. The distributions obtained by the geometric analysis for tortuosity (Fig. 11), pore radius (Fig. 12), and constriction factor (Fig. 13) are compared for the two considered scenarios. The main flow paths identified by the geometric (Fig. 14 and 16) and the hydraulic (Fig. 15, Fig. 17) approaches are shown for each flow direction (x, y, z)

In case 1, the isotropy is clearly visible from both the shortest paths obtained with the geometric approach (red lines) for each flowing direction (Fig. 14) and from the flow paths individuated
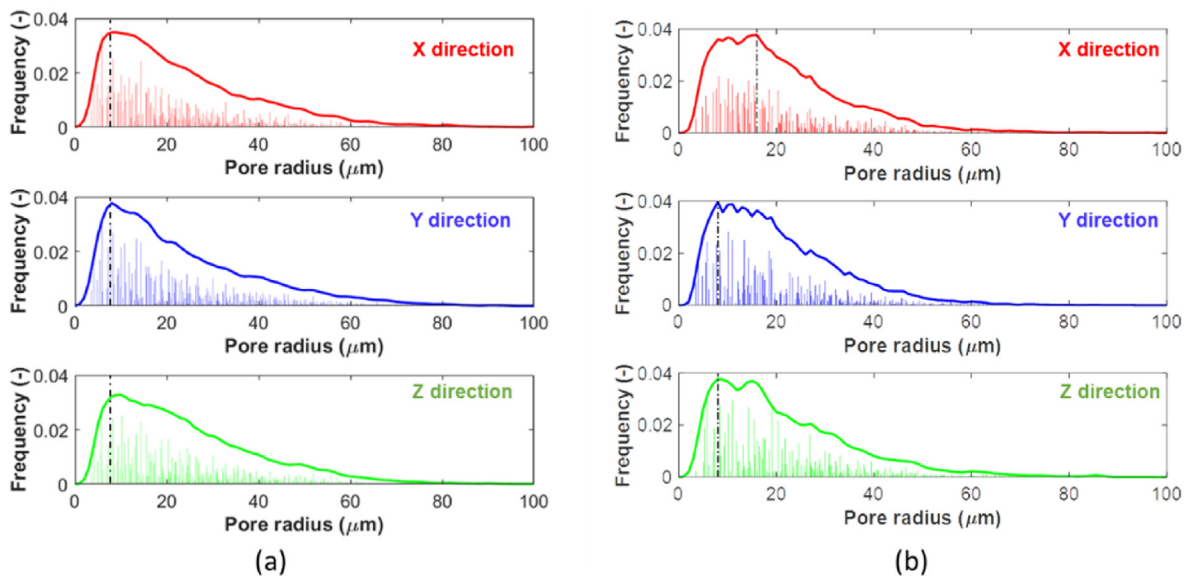

Fig. 12. Pore radius distribution and selected representative value (black dash-dot line) obtained from the geometric analysis in each flow direction: (a) case 1; (b) case 2.
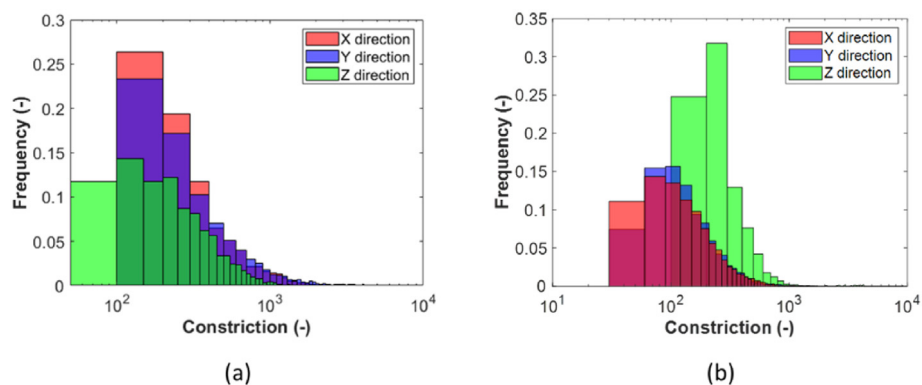

Fig. 13. Comparison of constriction factor of pores along paths in each direction: (a) case 1; (b) case 2.
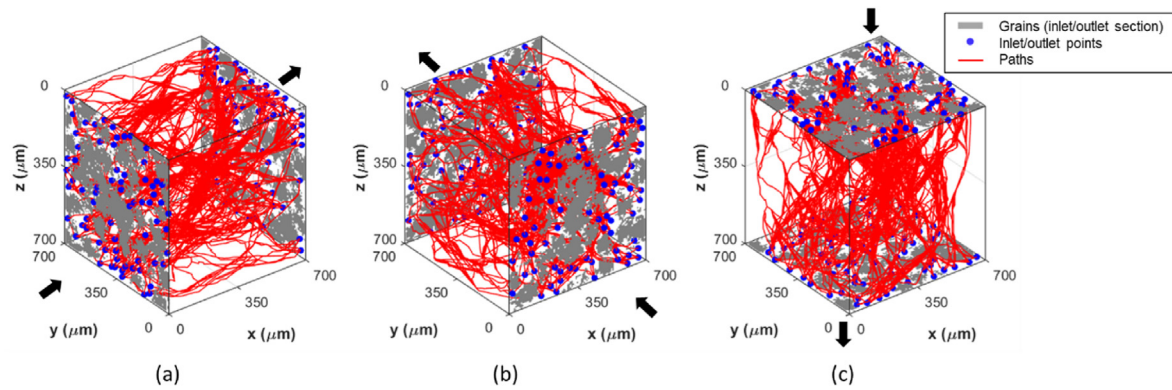
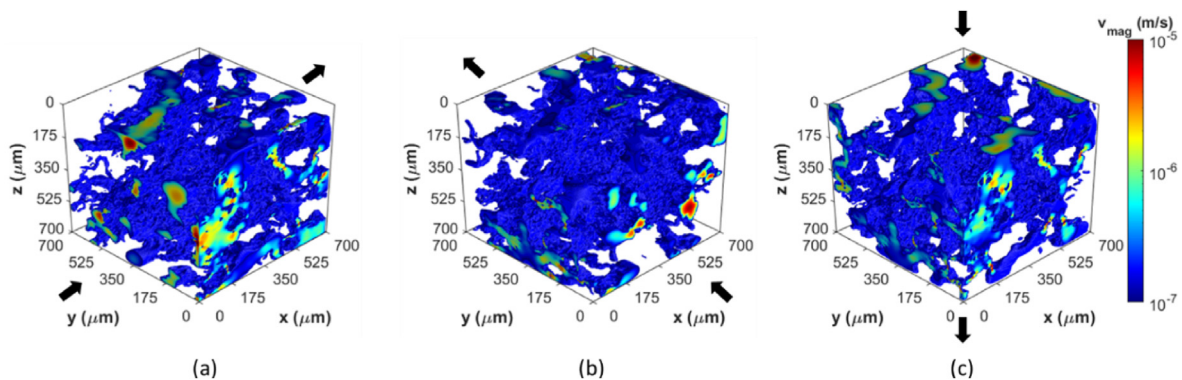Fig. 14. Detected geometric paths for case 1, considering flow in the $\boldsymbol{x}$ (a), $\boldsymbol{y}$ (b), and $\boldsymbol{z}$ (c) directions.

Fig. 15. Simulated velocity map ($|\boldsymbol{v}|$) for case 1 (fluid water), considering flow in the $\boldsymbol{x}$ (a), $\boldsymbol{y}$ (b), and $\boldsymbol{z}$ (c) directions.

through the velocity map resulting from the numerical simulation (Fig. 15). Quantitative estimates of permeability, anisotropy ratio, and effective porosity obtained by the two approaches are in good agreement (Table 3). The adopted value of the Kozeny-Carman coefficient $c_k = 5.8$ allowed an estimation of permeability values, in the three considered flow directions, in very good agreement with the calculated permeabilities from the hydraulic approach. The geometric tortuosity is comparable with the hydraulic tortuosity (discrepancy of 17%).

In case 2, the shortest paths, obtained with the geometric approach for each flowing direction (Fig. 16), are comparable with the flow paths individuated by the velocity map resulting from the numerical simulation (Fig. 17). By comparing Fig. 16c with Fig. 16a

and Fig. 16b, clear vertical anisotropy is visible, which is confirmed by quantitative estimates of effective porosity, tortuosity, and permeability in the horizontal vs. vertical direction (Table 3). The constriction factor is also much higher for the vertical direction (Fig. 13b). The Kozeny-Carman coefficient $c_k = 20$, obtained by fitting the permeability of the x and y directions with the values of the hydrodynamic simulation, is within the range of 4−40 reported in literature [30]. However, the calculated anisotropy is underestimated with respect to the one provided by the hydraulic approach (Table 3). This is partially due to the different estimations of tortuosity from the two approaches and from the potential effect of the constriction factor, which is not taken into account in the Kozeny-Carman expression.
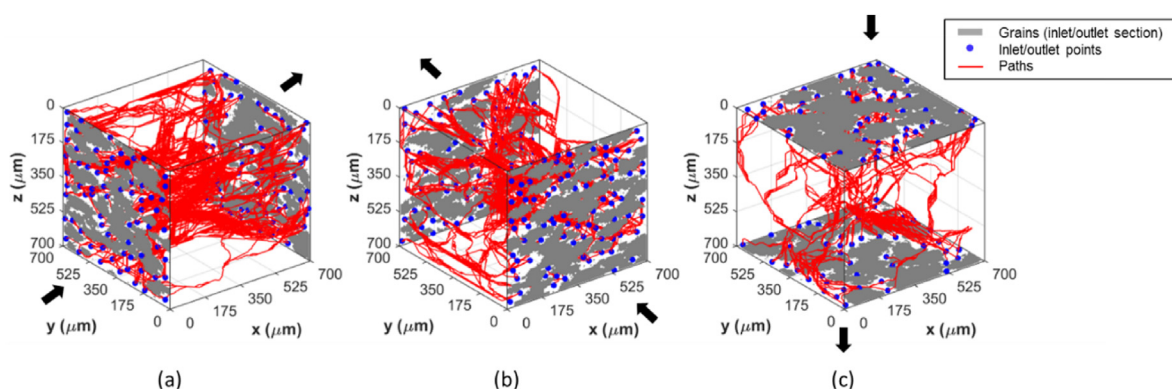

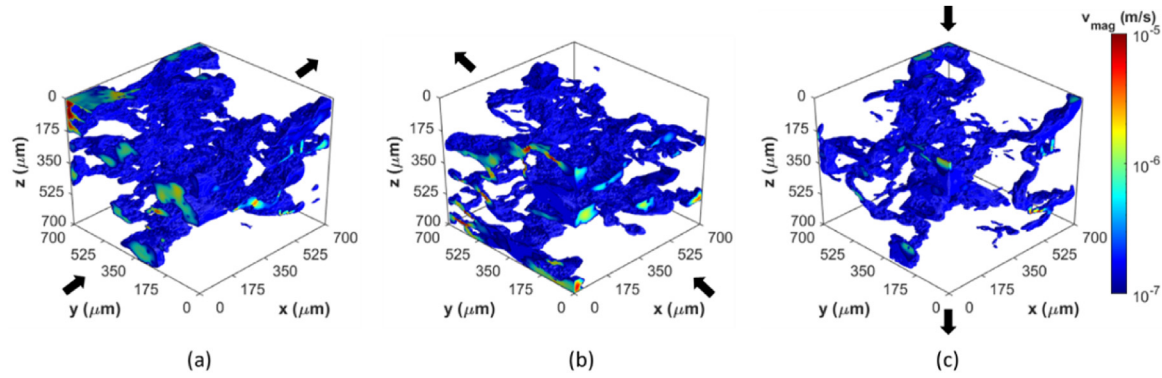Fig. 16. Detected geometric paths for case 2, considering flow in the $\boldsymbol{x}$ (a), $\boldsymbol{y}$ (b), and $\boldsymbol{z}$ (c) directions.

Fig. 17. Simulated velocity map (|**v**|) for case 2 (fluid water), considering flow in the **x** (a), **y** (b), and **z** (c) directions.

Table 4
Invariance of hydraulic characterization to the considered fluid in single-phase flow conditions (case 2).

		water	methane	heavy oil
Case 2	τ_x (−)	1.3204	1.3205	1.3204
	τ_y (−)	1.5195	1.5195	1.5195
	τ_z (−)	2.068	2.068	2.068
	φ_{ex}(%)	11.02	11.03	11.02
	φ_{ey}(%)	10.57	10.57	10.57
	φ_{ez}(%)	11.05	11.05	11.05
	k_x (mD)	662.8022	662.7746	662.8159
	k_y (mD)	286.526	286.511	286.5266
	k_z (mD)	71.611	71.6081	71.6129

The permeability values calculated from geometric data are strongly affected by the selected value of the Kozeny-Carman coefficient (c_k), which is difficult to be established a priori for irregular geometries such as anisotropic media. Moreover, the possibility to integrate constriction information in c_k, obtaining a tensorial representation of c_k, should be investigated. This would be in line with Katagiri et al. [57], who suggested the characterization of different shape factors for vertical and horizontal directions for anisotropic media.
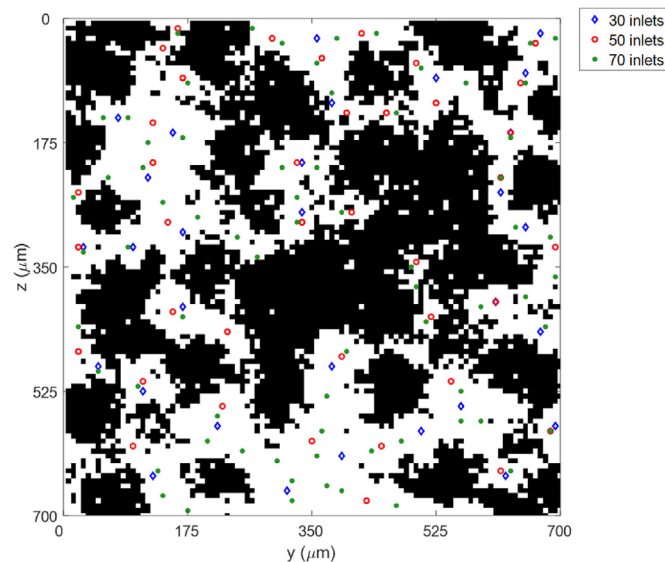

Fig. 18. Different inlet selections (x-direction): 30 points (blue diamonds), 50 points (red circles) and 70 points (green dots). (For interpretation of the references to colour in this figure legend, the reader is referred to the Web version of this article.)

The selection of the representative pore radius for each flow direction is also a sensitive choice. Square radius appears in eq. (9), therefore a small change in radius selection would correspond to a non-negligible change in permeability estimation.

The invariance of the hydrodynamic characterization to the considered fluid was verified. Fluids with very different properties such as water, gas (CH₄), and heavy oil were used for the hydraulic characterization of the anisotropic scenario. Comparable results were obtained for water, gas and heavy oil, as reported in Table 4. Thus, the proposed geometric approach can be effectively applied to a variety of scenarios characterized by single-phase flow, such as geothermal applications and aquifers, and to characterize petrophysical properties for gas storage scenarios, including CO_2 and H_2 storage, and reservoir production. Conversely, the proposed geometric approach cannot account for multiphase flow physics such as contact angle and interfacial tension, which result in relative permeability and capillary pressure effects at the macro scale. These properties may strongly affect the fluid motion and the preferential paths of the fluids. Further investigation must be carried out to account for multiphase flow phenomena.

The sensitivity of the geometric approach to the considered number and position of inlet/outlet pairs was investigated. For case 1 different inlet/outlet pairs were considered; the selected inlets on the x-z surface are shown in Fig. 18. As reported in Table 5, the methodology is robust. In fact, acceptable discrepancies were observed in terms of porosity and permeability values, while very similar values were obtained for pore radius and tortuosity in all the considered cases.

Finally, the impact of the porous geometry on the performance of the geometric approach was analyzed. The observed distribution of path depths, branching factors, and percentage of explored nodes are compared in Fig. 19 and Fig. 20 for case 1 and case 2, respectively, using 50 inlets/outlets per surface. As expected, for the more complicated pore geometry characterized by vertical anisotropy (case 2), path depth is usually greater in the vertical direction and a more extensive node exploration is required with respect to the isotropic case (case 1). However, some inlet points turned out to be connected to isolated pore volumes due to the joint effect of lower porosity and anisotropy. Therefore, when starting from such inlets, only few nodes (within 2%) are investigated, thus significantly reducing the overall computational time of case 2 with respect to case 1. For instance, by imposing 50 inlets/outlets per surface the running time of case 2 is 34% less than case 1.

Since the geometric approach is based on a prototype code implemented in Matlab which has not yet been optimized and/or parallelized, a quantitative comparison in terms of computational time against conventional CFD simulation (OpenFOAM) is not provided. Nevertheless, with the current prototype

Table 5
Robustness of the geometric characterization (case 1).

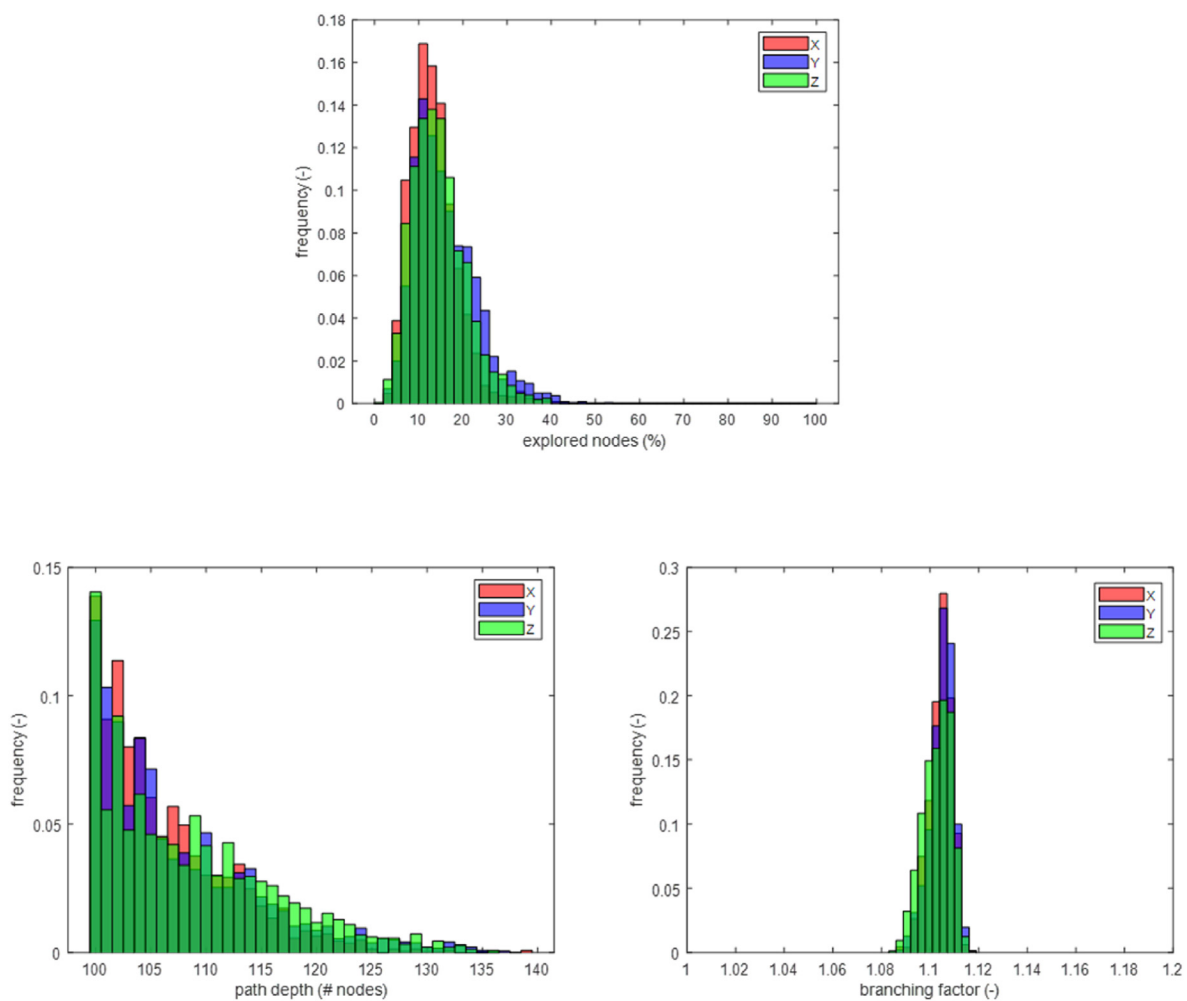|		30 inlet (outlet) per face	50 inlet (outlet) per face	70 inlet (outlet) per face
Case 1	τ_x (−)	1.37	1.35	1.34
	τ_y (−)	1.38	1.38	1.34
	τ_z (−)	1.36	1.4	1.31
	ϕ_{ex} (%)	15.2	16.7	15.6
	ϕ_{ey} (%)	15.3	16.9	15.5
	ϕ_{ez} (%)	17.5	19.0	18.3
	ϕ_e (%)	23.8	24.9	23.8
	r_x (μm)	7.7	6.9	7.6
	r_y (μm)	7.2	7.2	7.8
	r_z (μm)	7.7	7.3	7.8
	C_x	250	187	169
	C_y	110	120	122
	C_z	165	125	121
	k_x (mD)	836	759	885
	k_y (mD)	730	807	920
	k_z (mD)	985	906	1134

Fig. 19. Algorithm performance for case 1 (isotropic).

implementation, the computational time for geometric characterization is already lower than CFD single-phase simulation: run time reduction of about 5% considering 50 × 50 inlets/outlets per direction; run time reduction of about 80% less, considering 30 × 30 inlets/outlets per direction.

5. Conclusions

In this paper, a geometric analysis based on the A* path-finding algorithm is adopted to characterize the pore network geometry of 3D binary images representative of rock samples. Two synthetic validation cases, isotropic and anisotropic, were generated adopting the Quarter Structure Generation Set (QSGS) algorithm. A
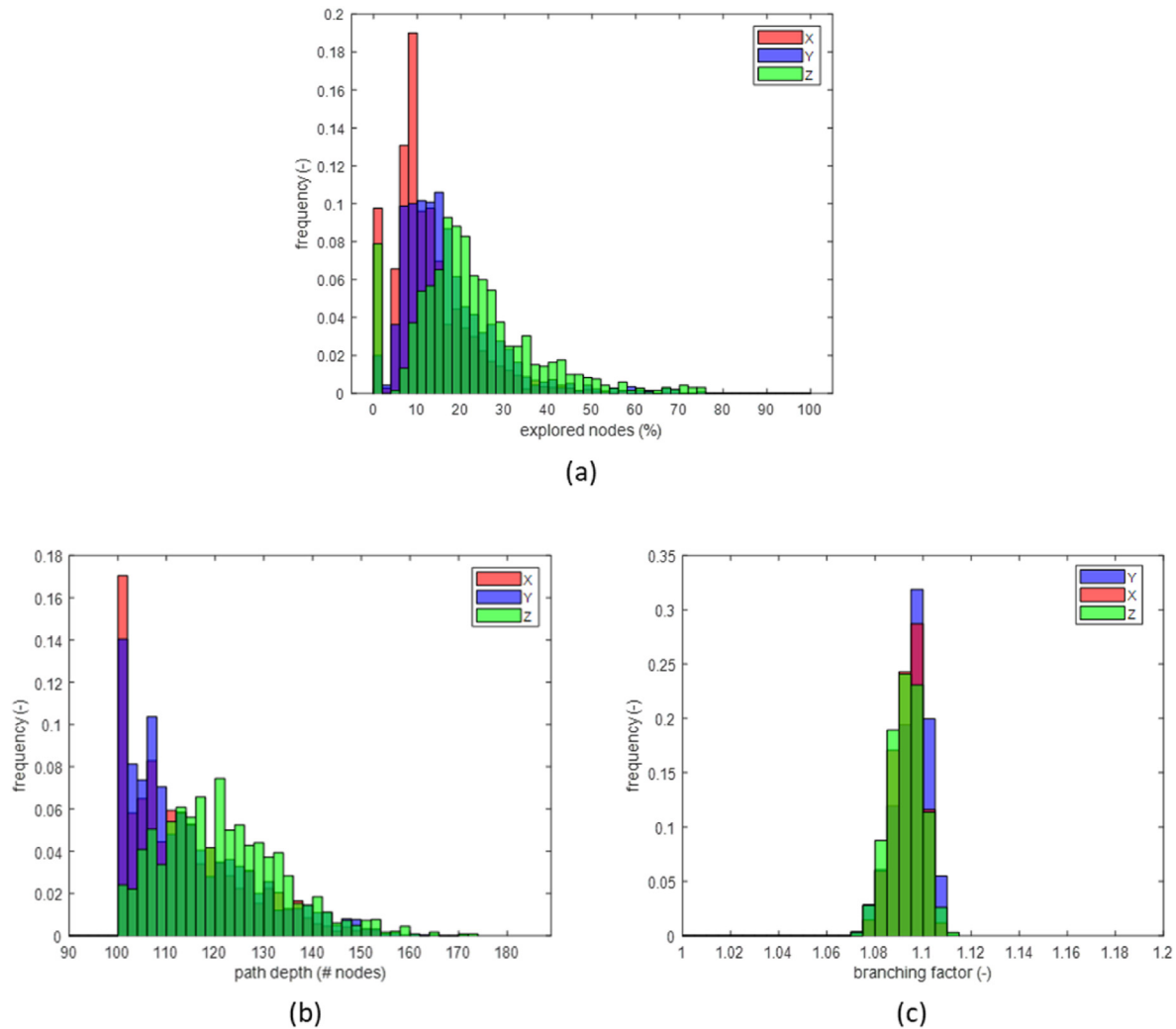
(a)

(b)

(c)

Fig. 20. Algorithm performance for case 2 (anisotropic).

preliminary automatic selection of inlet and outlet nodes for the six boundaries of the samples (two for each flow direction) was also proposed based on the medial axes algorithm. The A* algorithm searches for a path for each combination between all the selected inlet and outlet nodes for the three flow directions. For each identified path, a vector containing the local pore size is obtained. This information is used to produce a detailed description of the pore network and a tensorial representation of tortuosity, effective porosity, representative pore radius for calculation of permeability and anisotropy. To validate the results provided by the geometric approach we used a hydrodynamic CFD numerical simulator. Results showed that the path-finding approach could give a reasonable characterization of tortuosity, effective porosity, permeability, and anisotropy. Quantitative results obtained from the two approaches are in good agreement in both the isotropic and the anisotropic cases. Further studies on the characterization of representative pore radius and shape factor of the Kozeny Carman permeability equation could improve the accuracy and robustness of permeability and anisotropy estimate.

Sensitivity analysis showed that the algorithm is quite robust with respect to the selected number of inlets/outlets.

Both pore structure and the selected number of inlets/outlets per direction have an impact on computational time. Compared to the CFD simulation, computational times turned out to be

competitive and very promising considering that the implemented algorithm had not yet been parallelized nor optimized.

The developed geometric approach can be effectively applied for a thorough description and characterization of the internal geometry of porous media in terms of pore radius distribution and texture parameters, providing useful information for a number of applications such as effective diffusion coefficient calculation, effect of weathering in ornamental stones, and, as discussed in this paper, geometrical calculation of permeability and anisotropy. As a consequence, it can be useful for a variety of scenarios such as geothermal applications, gas storage, including CO_2 and H_2, and reservoir production. Furthermore, from the computational point of view, the algorithm is extremely suitable for an efficient parallelization since each path is calculated independently.

On the other hand, since it does not account for contact angle and interfacial tensions, relative permeability and capillary pressure cannot be characterized. The proposed methodology should not be considered as an alternative to conventional CFD simulation but as a possible additional tool for thorough geometrical description and characterization of the pore network geometry.

Credit author statement

Eloisa Salina Borello Methodology, Software, Formal analysis,

Visualization, Writing. **Costanzo Peter** Methodology, Software, Validation, Writing. **Filippo Panini** Methodology, Validation, Visualization, Writing. **Dario Viberti;** Conceptualization, Methodology, Supervision, Writing − review & editing.

Declaration of competing interest

The authors declare that they have no known competing financial interests or personal relationships that could have appeared to influence the work reported in this paper.

Nomenclature

Symbol Quantity SI unit

AR	aspect ratio ($D_z/D_{x,y}$)	
b	branching factor	
c	cost function m	
c_d	Connectivity distance	
c_k	Kozeny-Carman coefficient	
C	constriction factor	
d	path depth	
D_i	growth probability in the i-direction	
g	backward cost m	
h	forward cost m	
k_g	permeability from the geometric calculation m^2	
k_h	permeability from the hydraulic simulation m^2	
L_i	sample length in the i-direction m	
L_p	pore channel length m	
L_{sh}	length of the shortest path m	
p	pressure Pa	
P	core distribution probability	
r_e	equivalent radius m	
r_h	hydraulic radius m	
r_i	mean pore radius in the i-direction m	
r_p	local pore radius m	
R	anisotropy ($k_{x,y}/k_z$)	
u	Darcy velocity m/s	
v	local velocity m/s	
ϕ	total porosity	
ϕ_e	effective porosity	
μ	viscosity Pa s	
τ_g	geometric tortuosity	
τ_h	hydraulic tortuosity	

Abbreviations

A*	A-star algorithm
QSGS	Quarter Structure Generation Set
CFD	Computational fluid dynamics
FVM	Finite volume method

Appendix A. automatic selection of inlets and outlets

Since the boundary faces of a 3D binary image of a porous medium can be characterized by a significant number of small pores, a manual selection of inlet and outlet nodes for each flow direction can be inefficient and time-consuming. For this reason, we developed an algorithm for automatic inlet/outlet nodes placement. The algorithm is based on the medial axis approach. It exploits the implementation of the Matlab Image Processing Toolbox to extract the skeleton (S) of the pore network on the 2D images representing the boundary faces. Points of the skeleton are then clustered following the K-means algorithm; the number of clusters is fixed to the desired number of inlets/outlets. From each cluster, the cell centroid nearest to the cluster centroid is selected as

an inlet/outlet point. This way, the selected inlet/outlet points lay in the middle of the pore (belonging to medial axes) and are spread almost uniformly on the pore domain. For example, Fig. A1 shows a 2D inlet surface of a synthetic porous medium characterized by numerous small pores; the skeleton of the corresponding pore space network is depicted in cyan; 150 automatically individuated inlet points are depicted in blue.
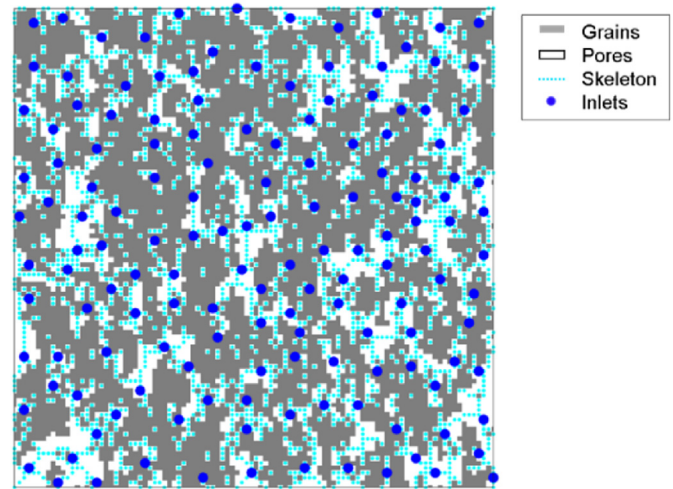

Fig. A1. Example of a boundary surface with automatic identification of inlets.

Appendix B. calculation of pore size

Along each path individuated by the A* algorithm, for each point $P_i = (x_i, y_i, z_i)$, the flow direction is calculated as the direction vector v_i joining P_i with the adjacent point P_{i+1}, i.e. $v_i = (x_{i+1} - x_i, y_{i+1} - y_i, z_{i+1} - z_i)$. Components of v_i can be pictured as the slopes of the projections of the line onto each of the three coordinate planes. The corresponding unit vector $\widehat{v_i} = (a, b, c)$ is obtained by dividing each component of v_i by $|v_i|$. In order to reduce the computational cost, attention is limited to a finite number of possible directions:

- along main axes (ex. 1,0,0)
- along 2D planes with slope 1 or -1 (ex. $1/\sqrt{2}, 1/\sqrt{2}, 0$)
- in the 3D space with the same absolute value for each component (ex. $1/\sqrt{3}, 1/\sqrt{3}, -1/\sqrt{3}$).

To this end, $\widehat{v_i}$ is associated with the most similar unit vector in the considered discretized set, neglecting the sign. Successively, the orthogonal plane crossing the current point is calculated as:

$$a(x - x_i) + b(y - y_i) + c(z - z_i) = 0 \qquad (B.1)$$

Two mutually perpendicular directions (n_1 and n_2), belonging to the orthogonal plane, are selected to compute the pore extensions, called d_1 and d_2, respectively; d_1 (or d_2) are calculated by moving forward and backward along n_1 (or n_2) from P_i until grains are reached (Fig. 6). Pore radius (r_p) is thus approximated by the radius of the equivalent circumference, i.e. the circumference with an area equivalent to the ellipse of diameters d_1 and d_2:

$$r_p = \frac{1}{2}\sqrt{d_1 d_2} \qquad (B.2)$$

Finally, an estimate of pore eccentricity is given by:

$$e = \frac{\sqrt{d_1^2 - d_2^2}}{d_1} \tag{B.3}$$

References

[1] Satter A, Varnon JE, Hoang MT. Integrated reservoir management. J Petrol Technol 1994;46:1057−64. https://doi.org/10.2118/22350-PA.

[2] Verga F. What's conventional and what's special in a reservoir study for underground gas storage. Energies 2018;11(Issue 5). https://doi.org/10.3390/en11051245.

[3] Cui G, Pei S, Rui Z, Dou B, Ning F, Wang J. Whole process analysis of geothermal exploitation and power generation from a depleted high-temperature gas reservoir by recycling CO2. Energy, Elsevier 2021;217(C). https://doi.org/10.1016/j.energy.2020.119340.

[4] Rocca V, Viberti D. Environmental sustainability of oil industry. Am J Environ Sci 2013;9:210−7. https://doi.org/10.3844/ajessp.2013.210.217. ISSN:1553-345X.

[5] Benetatos C, Viberti D. Fully integrated hydrocarbon reservoir studies: myth or reality? Am J Appl Sci 2010;7(11):1477−86. https://doi.org/10.3844/ajassp.2010.1477.1486.

[6] Fokker P, Salina Borello E, Verga F, Viberti D. Harmonic pulse testing for well performance monitoring. Journal of petroleum science and engineering, vol. 162. Elsevier; 2018. p. 446−59. https://doi.org/10.1016/j.petrol.2017.12.053.

[7] Panini F, Onur M, Viberti D. An analytical solution and nonlinear regression analysis for sandface temperature transient data in the presence of a near-wellbore damaged zone. Transport Porous Media 2019;129(3):779−810.

[8] Peter C, Sacchi Q, Salina Borello E. Study of reservoir production uncertainty using channel amalgamation. Geoingegneria ambientale e mineraria (GEAM), vol. 146. Pàtron Editore S.r.l; 2015. p. 53−64. 3.

[9] Peter C, Salina Borello E, Dalman R, Karamitopoulos P, Busschers F, Sacchi Q, Verga F. Improved lithology prediction in channelized reservoirs by integrating stratigraphic forward modeling: towards improved model calibration in a case study of the Holocene Rhine-Meuse fluvio-deltaic system. Comput Geosci 2019;141. https://doi.org/10.1016/j.cageo.2020.104517. Elsevier.

[10] Salina Borello E, Fokker PA, Viberti D, Verga F, Hofmann H, Meier P, Min K-B, Yoon K, Zimmermann G. Harmonic pulse testing for well monitoring: application to a fractured geothermal reservoir. Water resources research, vol. 55. AGU Publications. Wiley.; 2019. p. 4727−44. https://doi.org/10.1029/2018WR024029. 6.

[11] Verga F, Viberti D, Salina Borello E. A new insight for reliable interpretation and design of injection tests. Journal of petroleum science and engineering, vol. 78. Elsevier; 2011. p. 166−77. https://doi.org/10.1016/j.petrol.2011.05.002. - ISSN 0920-4105 - doi:.

[12] Verga F. Salina Borello E.: unconventional well testing: a brief overview. Geoingegneria ambientale e mineraria (GEAM), vol. 149. Pàtron Editore S.r.l; 2016. p. 45−54. 3.

[13] Viberti D, Cossa A, Galli MT, Pirrone M, Salina Borello E, Serazio C. A novel approach to a quantitative estimate of permeability from resistivity log measurements. Geoingegneria ambientale e mineraria (GEAM), vol. 155. Pàtron Editore S.r.l; 2018. p. 17−24. 3.

[14] Horne RN. Uncertainty in well test interpretation. SPE-27972-MS. In: University of Tulsa centennial petroleum engineering symposium, 29-31 august, Tulsa, Oklahoma; 1994. https://doi.org/10.2118/27972-MS.

[15] Viberti D. A rigorous mathematical approach for petrophysical properties estimation. Am J Appl Sci 2010;7(11):1509−16. https://doi.org/10.3844/ajassp.2010.1509.1516. - ISSN 1546-9239.

[16] Viberti D, Verga F. An approach for the reliable evaluation of the uncertainties associated to petrophysical properties, mathematical geosciences. Springer 2012;4(Issue 3):327−41. https://doi.org/10.1007/s11004-011-9358-1.

[17] Bear J. Dynamics of fluids in porous media. Courier Corporation; 2013.

[18] Ghanbarian B, Hunt AG, Ewing RP, Sahimi M. Tortuosity in porous media: a critical review. Soil Sci Soc Am J 2013;77(5):1461−77.

[19] Carman PC. Fluid flow through granular beds. Trans Inst Chem Eng 1937;15:150−66.

[20] Adler P. Porous media: geometry and transports. Elsevier; 2013.

[21] Clennell MB. Tortuosity: a guide through the maze. Geol Soc London Spec Publ 1997;122(1):299−344.

[22] Koponen A, Kataja M, Timonen J. Permeability and effective porosity of porous media. Phys Rev 1997;56(3):3319.

[23] Tu J, Yeoh GH, Liu C. Some advanced topics in CFD. Comput Fluid Dynamic 2018:369−417.

[24] Berg CF. Permeability description by characteristic length, tortuosity, constriction and porosity. Transport Porous Media 2014;103(3):381−400.

[25] Gostick JT. Versatile and efficient pore network extraction method using marker-based watershed segmentation. Phys Rev 2017;96(2). https://doi.org/10.1103/PhysRevE.96.023307.

[26] Sheppard AP, Sok RM, Averdunk H. Techniques for image enhancement and segmentation of tomographic images of porous materials. Phys A Stat Mech Appl 2004;339(1):145−51.

[27] Rabbani A, Mostaghimi P, Amstrong TA. Pore network extraction using geometric domain decomposition. Adv Water Resour 2014;123:70−83. https://doi.org/10.1016/j.advwatres.2018.11.003. Elsevier.

[28] Xu Z, Lin M, Jiang W, Cao G, Yi Z. Identifying the comprehensive pore structure characteristics of a rock from 3D images. J Petrol Sci Eng 2020;187:106764. https://doi.org/10.1016/j.petrol.2019.106764. 0920-4105.

[29] Xu P, Yu B. Developing a new form of permeability and Kozeny−Carman constant for homogeneous porous media by means of fractal geometry. Adv Water Resour 2008;31(1):74−81. https://doi.org/10.1016/j.advwatres.2007.06.003. ISSN 0309-1708.

[30] Xiao B, Wang W, Zhang X, Long G, Fan J, Chen H, Deng L. A novel fractal solution for permeability and Kozeny-Carman constant of fibrous porous media made up of solid particles and porous fibers. Powder Technol 2019;349:92−8. https://doi.org/10.1016/j.powtec.2019.03.028. 2019, ISSN 0032-5910.

[31] Cai J, Zhang Z, Wei W, Guo D, Li S, Zhao P. The critical factors for permeability-formation factor relation in reservoir rocks: pore-throat ratio, tortuosity and connectivity. Energy, Elsevier 2019;188:116051. https://doi.org/10.1016/j.energy.2019.116051. ISSN 0360-5442.

[32] Liu J, Regenauer-Lieb K. Application of percolation theory to micro-tomography of rocks. Earth Sci Rev 2021;214. https://doi.org/10.1016/j.earscirev.2021.103519. Part A, 2014.

[33] Lindquist WB, Lee SM, Coker DA, Jones KW, Spanne P. Medial axis analysis of void structure in three-dimensional tomographic images of porous media. J Geophys Res: Solid Earth 1996;101(B4):8297−310.

[34] Al-Raoush RI, Madhoun IT. TORT3D: a MATLAB code to compute geometric tortuosity from 3D images of unconsolidated porous media. Powder Technol 2017;320:99−107.

[35] Liang Y, Hu P, Wang S, Song S, Jiang S. Medial axis extraction algorithm specializing in porous media. Powder Technol 2019;343:512−20. https://doi.org/10.1016/j.powtec.2018.11.061. ISSN 0032-5910.

[36] Sun WC, Andrade JE, Rudnicki JW. Multiscale method for characterization of porous microstructures and their impact on macroscopic effective permeability. Int J Numer Methods Eng 2011;88(12):1260−79.

[37] Prodanović M, Lindquist WB, Seright RS. Porous structure and fluid partitioning in polyethylene cores from 3D X-ray microtomographic imaging. J Colloid Interface Sci 2006;298(1):282−97. https://doi.org/10.1016/j.jcis.2005.11.053.

[38] Martell V, Sandberg A. Performance evaluation of A* algorithms. Karlskrona, Sweden: Blekinge Institute of Technology; 2016. Dissertation.

[39] Wang M, Wang J, Pan N, Chen S. Mesoscopic predictions of the effective thermal conductivity for microscale random porous media. Phys Rev E 2007;75(3):036702.

[40] Guibert R, Nazarova M, Horgue P, et al. Computational permeability determination from pore-scale imaging: sample size, mesh and method sensitivities. Transport Porous Media 2015;107:641−56. https://doi.org/10.1007/s11242-015-0458-0.

[41] Chen L, Kang Q, Viswanathan HS, Tao W-Q. Pore-scale study of dissolution-induced changes in hydrologic properties of rocks with binary minerals. Water Resour Res 2014;50(12):9343−65.

[42] Chen L, Kang Q, Dai Z, Viswanathan HS, Tao W. Permeability prediction of shale matrix reconstructed using the elementary building block model. Fuel 2015;160:346−56.

[43] Germanou L, Ho MT, Zhang Y, Wu L. Intrinsic and apparent gas permeability of heterogeneous and anisotropic ultra-tight porous media. J Nat Gas Sci Eng 2018;60:271−83. https://doi.org/10.1016/j.jngse.2018.10.003. ISSN 1875-5100.

[44] Zhou Y, Yan C, Tang AM, Duan C, Dong S. Mesoscopic prediction on the effective thermal conductivity of unsaturated clayey soils with double porosity system. Int J Heat Mass Tran 2019;130:747−56.

[45] Wang M, Chen S. Electroosmosis in homogeneously charged micro and nanoscale random porous media. J Colloid Interface Sci 2007;314(1):264−73.

[46] Wang Z, Jin X, Wang X, Sun L, Wang M. Pore-scale geometry effects on gas permeability in shale. J Nat Gas Sci Eng 2016;34. https://doi.org/10.1016/j.jngse.2016.07.057.

[47] Tian J, Qi C, Sun Y, Yaseen ZM, Pham BT. Permeability prediction of porous media using a combination of computational fluid dynamics and hybrid machine learning methods. Eng Comput 2020. https://doi.org/10.1007/s00366-020-01012-z.

[48] WoessnerW, Poeter E. Hydrogeologic properties of earth materials and principles of groundwater flow. Guelph, Ontario, Canada: Published by the Groundwater Project; 2020.

[49] Jin Yi, Wang Cheng, Liu Shunxi, Quan Weizhe, Liu Xiaokun. Systematic definition of complexity assembly in fractal porous media journals, vol. 28; 2020. p. 2050079. 05, 10.1142/S0218348x20500796. 10.1142/S0218348X20500796.

[50] Viberti D, Peter C, Borello ES, Panini F. Pore structure characterization through path-finding and Lattice Boltzmann simulation. Adv Water Resour 2020: 103609.

[51] Hart PE, Nilsson NJ, Raphael B. A formal basis for the heuristic determination of minimum cost paths. IEEE Trans Syst Sci Cybern 1968;4(2):100−7.

[52] Nilsson NJ. Principles of artificial intelligence. Morgan Kaufmann; 2014.

[53] Russell SJ, Norvig P. Artificial intelligence a modern approach. Boston: Pearson; 2018. ISBN 978-0134610993. OCLC 1021874142.

[54] Mauran S, Rigaud L, Coudevylle O. Application of the Carman−Kozeny Correlation to a high-porosity and anisotropic consolidated medium: the compressed expanded natural graphite. Transport Porous Media 2001;43:355−76.

https://doi.org/10.1023/A:1010735118136.

[55] Clavaud J-B, Maineult A, Zamora M, Rasolofosaon P, Schlitter C. Permeability anisotropy and its relations with porous medium structure. J Geophys Res 2008;113:B01202. https://doi.org/10.1029/2007JB005004.

[56] Wyllie MRJ, Spangler MB. Application of electrical resistivity measurements to problem of fluid flow in porous media. AAPG (Am Assoc Pet Geol) Bull 1952;36(2):359−403.

[57] Katagiri J, Kimura S, Noda S. Significance of shape factor on permeability anisotropy of sand: representative elementary volume study for pore-scale analysis. Acta Geotech 2020;15:2195−203. https://doi.org/10.1007/s11440-020-00912-0.

[58] Ferrari A, Lunati I. Direct numerical simulations of interface dynamics to link capillary pressure and total surface energy. Adv Water Resour 2013;57:19−31.

[59] Soulaine C, Gjetvaj F, Garing C, Roman S, Russian A, Gouze P, Tchelepi HA. The impact of sub-resolution porosity of X-ray microtomography images on the permeability. Transport Porous Media 2016;113(1):227−43.

[60] Rahmanian M, Kantzas A. Stochastic generation of virtual porous media using a pseudo-crystallization approach. J Nat Gas Sci Eng 2018;53:204−17.

[61] Patankar SV. Numerical heat transfer and fluid flow. Washington DC: Taylor & Francis; 1980.

[62] Koponen A, Kataja M, Timonen JV. Tortuous flow in porous media. Phys Rev 1996;54(1):406.

[63] Aminpour M, Galindo-Torres SA, Scheuermann A, Li L. Pore-scale behavior of Darcy flow in static and dynamic porous media. Phys Rev Appl 2018;9(6):064025.

[66] Li T, Li M, Jing X, Xiao W, Cui Q. Influence mechanism of pore-scale anisotropy and pore distribution heterogeneity on permeability of porous media. Petrol Explorat Dev 2019;46(3):594−604. https://doi.org/10.1016/S1876-3804(19)60039-X.

[67] Li K, Horne R. Fractal Characterization of the geysers rock. Trans Geoth Resour Counc 2021;27.

[68] Øren P, Bakke S. Reconstruction of Berea sandstone and pore-scale modelling of wettability effects. J Petrol Sci Eng 2003;39(3−4):177−99.